Activity report of the Italian CRG beamline at the European Synchrotron Radiation Facility (ESRF)

N 11, Jan 2024
Grenoble, Jan 2024

71 Avenue des Martyrs, Grenoble, France

Editorial manager: Francesco d'Acapito (*dacapito@iom.cnr.it*)
ISSN 2553-9248
DOI: 10.5281/zenodo.10356771

Abstract
This document resumes the activity of the Italian CRG beamline at ESRF (LISA project) during year 2023. The latest news from the beamline are presented as well as details on the technical activity, highlight experiments and publications.

Keywords
Italian beamline at ESRF, BM08
LISA project
X-ray Absorption Spectroscopy

Table of Contents

Foreword

The year 2023 witnessed a high level of activity at LISA, characterized by a significant presence of users and students visiting the beamline. LISA has provided 368 shifts of beamtime in User Mode, out of which 246 to ESRF users and 122 to CERIC users. In total, 28 experiments have been carried out, 18 in the ESRF quota and 10 in the CERIC quota. The distribution of the scientific areas and the distribution of the Main Proposer (MP) nationalities of the experiments are shown in Figure 1

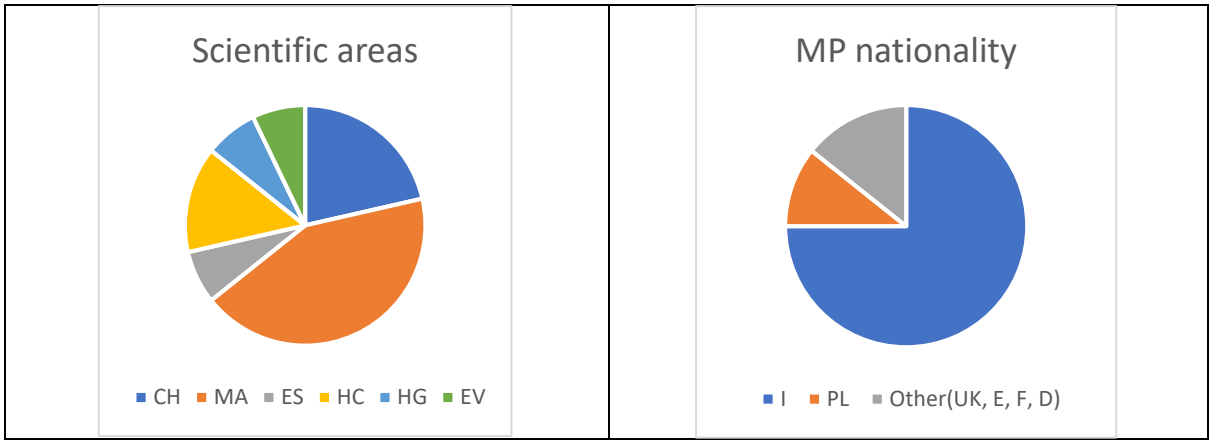

Figure 1: Statistics on the experiments carried out in 2023 at LISA. ***Left****: Scientific areas* ***Right****: nationality of the Main Proposers.*

From Figure 1 it is evident that MA (Applied Materials Science) is the dominating area, and that the Italian community is markedly present at LISA, followed by the Polish community.

During 2023 LISA has experienced two major failures of the instrumentation. First: a crack in the cooling pipe of the upper principal slit (Figure 2). This has led to a complete flooding of the first vacuum chamber of the beamline.

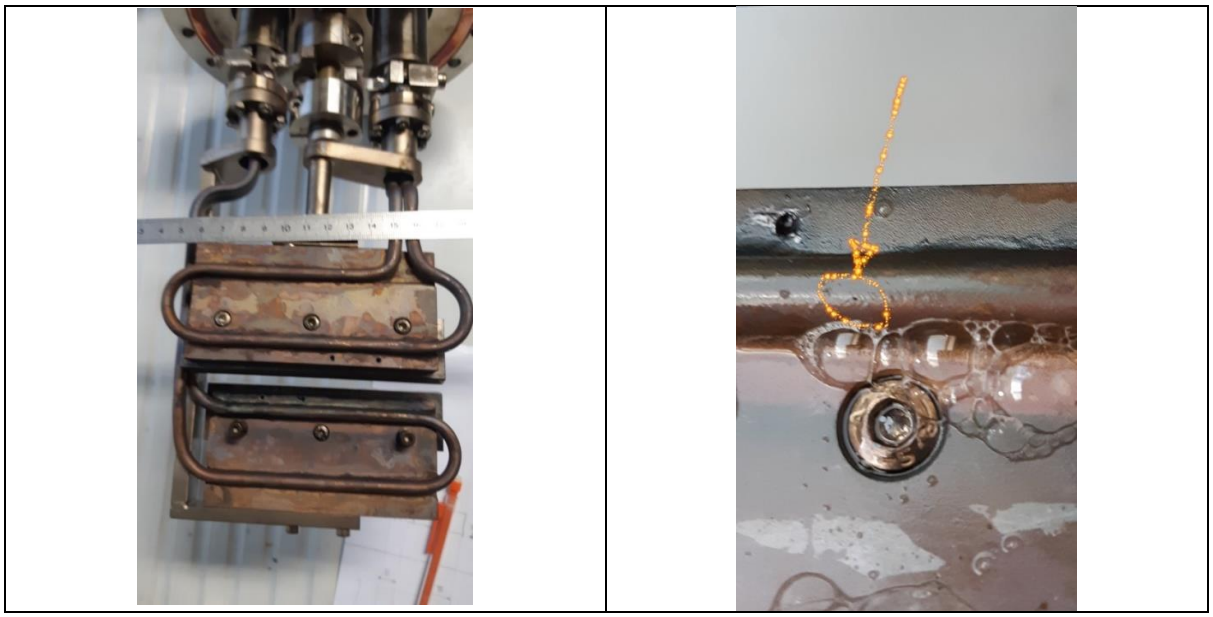

Figure 2: Pictures of the damaged principal slits. ***Left****: the whole group showing the slits and the copper tubes bringing the cooling water;* ***Right*** *the crack on the tube evidenced by the circle and the arrow.*

Second, a failure of the Liquid Nitrogen (LN) main admission valve to the Phase separator. Both accidents lead to a complete stop of the beamline operations for about 5 weeks and 5 experiments had to be cancelled. However, with the help of the ESRF CRG office and technical services and the rapid intervention of the manufacturer of the LN line, the lost beamtime could be rescheduled within the 2023 run4 and 5 periods (the latter ending next Feb 29 2024).

Concerning agreements and projects LISA has been particularly active this year with the following results:

- Agreement with the Milano Bicocca University for hosting at LISA a post doc dedicated to studies on materials for batteries and cultural heritage. Dr Jacopo Orsilli was awarded the position and now he is part of the LISA staff.
- Agreement with the Bologna University for a collaboration on photochemistry. The agreement foresees an RTD-A position working in part at LISA and the selection procedure is in progress.
- Project CECOMEC. Project financed by CERIC, is focused on the production and characterization of materials for Solid Oxide Fuel Cells based on ceria. The project foresees hiring a post Doc working at LISA for 3 years, the call for candidatures will be published in the forthcoming weeks.

In addition, LISA has hired a collaborator (Alessandro Puri) for tasks focused on calibration of the optical elements of the beamline and has hosted several PhD students:

- First semester: Simone Amatori (Univ. Roma Tre), Matilde Ciani (Univ. Firenze), Eleni Petsali (Univ. Thessaloniki, Gr).
- Second semester: Raffaele Russo (Univ. Camerino), Simone Margheri (Univ. Firenze).

News from the beamline

Micro-sized samples

A new calibration of the monochromator movements carried out recently has led to an increased spatial stability of the focused beam. This has opened the opportunity to the analysis of micro-sized samples (tens of μm). Here it is shown an example of a study conducted on an Yb-doped silicate optic fiber with a core with a diameter of 10μm (collaboration with Prof. W. Blanc, Nice University, see Lu et al. Optical materials 2023 DOI: 10.1016/j.optmat.2023.113644).

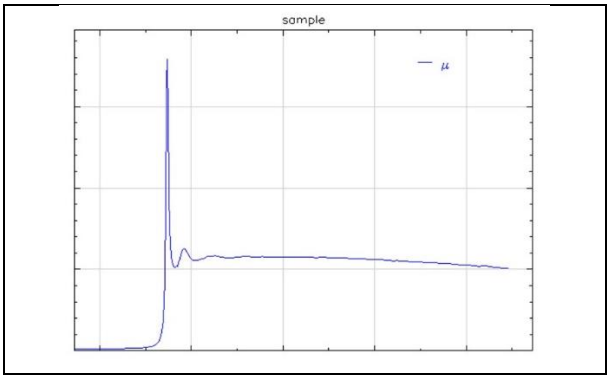

Figure 3: EXAFS spectrum at the Yb- L3 edge of a silicate fibre. The dopant is contained only in the core which has a diameter of 10μm and the doping level is below 1 at %. The average of 8 XAS spectra is shown for a total time of 8 hours.

This result proves the high spatial stability of the beam position also in the long term and it opens the way to the study of samples even below the size of the beam.

Infrastructural interventions

During year 2023 two relevant interventions on safety have been carried out. The first one consisted in the installation of a 'passerelle' (Figure 4, left) above the last control cabin of the beamline (stores) for accessing the main manual admission valve of the Liquid Nitrogen line. This will make easier and safer any action on this valve in the case of a failure or a technical intervention on the Liquid Nitrogen circuit.

Figure 4: Pictures of the interventions carried out at LISA this year. ***Left****; the 'passerelle' giving access to the main admission valve of the Liquid Nitrogen distribution line.* ***Right****: the new floor-covering in the LISA chemistry lab.*

The second intervention consisted in the renewal of the floor covering in the chemical lab of LISA that, after 25 years of use, presented several cracks and uncovered zones, posing potential safety risks. Now the floor is smooth and shiny as shown in Figure 4, right.

New Beamline Manual

A recently released user manual is now online and it is designed to assist users in their typical activities at the beamline (see Figure 5)Figure 5: The new LISA user guide. It provides details about the beamline instrumentation and includes essential information for conducting experiments. It is highly recommended that users familiarize themselves with the manual before their visit to the beamline. You can access and download the manual from the following page:
https://www.esrf.fr/UsersAndScience/Experiments/CRG/BM08/Users

Figure 5: The new LISA user guide

New Beamline Software

A new release of the data reduction application, dconv_multiV4, is now available to the users (see Figure 6). This application generates an ASCII file that includes calibrated energy and essential counters crucial for data analysis. To function correctly, the app requires the *dconv_configV4.txt* configuration file, which should be located in the same directory as the main program. You can obtain the Windows executable, the configuration file, and the Python script bundled in an archive by visiting the following address:
https://cloud.esrf.fr/s/AwBNPsck4CJBB5Z
More info, including the readme file can be found at:
https://github.com/Puri-a/dconv_multi/tree/main/dconv_multiV4

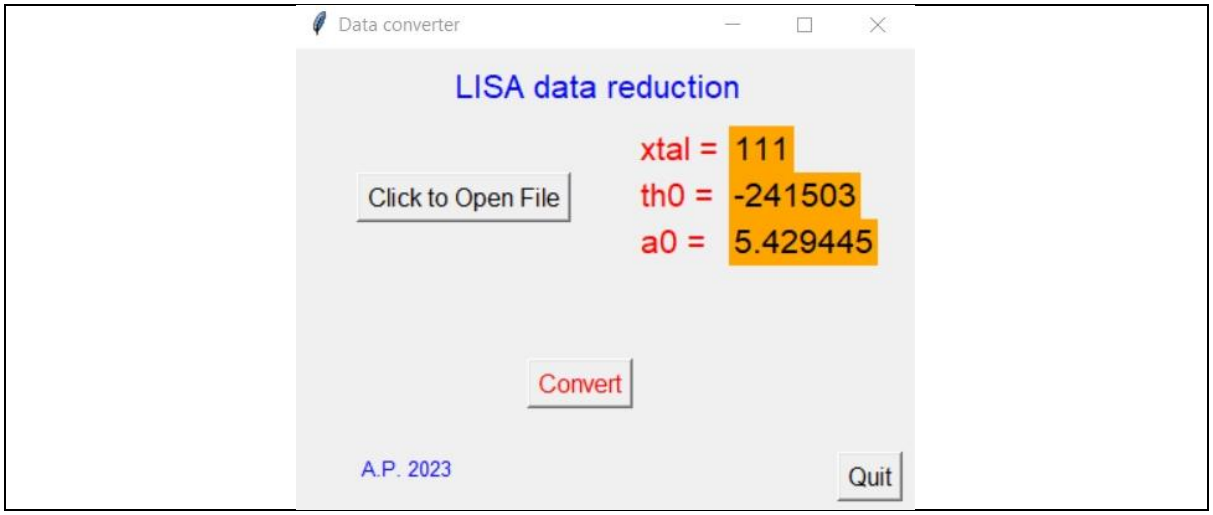

Figure 6: dconv_multiV4 application main screen

Social events

During year 2023 LISA has hosted a series of events oriented to dissemination of the scientific activity of the beamline to the general public. On Dec 5th the ESRF and our beamline have been visited by the Italian general consul in Lyon, C. Petracca (Figure 7) whereas on Dec 13th high school students from the local "Cité Scolaire Intérnationale" visited the site and LISA.

Figure 7: A. Puri presenting the beamline to the Italian General Consul in Lyon, C. Petracca (credits D. Chenevier, ESRF).

Doctorate students' activity

Gold Nanorods derivatized with CTAB and Hydroquinone or Ascorbic Acid: Spectroscopic Investigation of Anisotropic Nanoparticles of different shape and size

S. Amatori (a), A. Lopez (a), C. Meneghini (a), A. Calcabrini (b), M. Colone (b), A. Stringaro (b), S. Migani (b), I. Khalakhan (c), G Iucci (a), I. Venditti (a) and C. Battocchio (a)
a) Dept. of Sciences, Roma Tre University, Rome, Italy b) National Center for Drug Research and Evaluation, Istituto Superiore di Sanità, Rome, Italy c) Dept. of Surface and Plasma Science, Charles University, Prague, Czech Republic

Gold Nanomaterials are attracting a lot of interest in the latest decades thanks to their peculiar physicochemical properties that arise from their high surface-to-volume ratio and their unique Surface Plasmon Resonance. The potential applications in several fields, ranging from sensors to biomedicine, emerges from the ability to tailor these materials in order to obtain the desired properties for each application, such as shape and dimensions (that can in turn modify the optical properties) and choice of capping ligand, which can modify stability (prevent/allow aggregation under specific conditions), as well as solubility (hydro/lipo-philic nature) and chemical reactivity (es. exposing a specific chemical group via surface functionalization) of these systems. Among others, anisotropic (i.e. non-spherical) particles have attracted much attention due to their size- and shape-dependent optical properties and rod-shaped nanoparticles are particularly interesting since they display two plasmon bands: a transverse plasmon band corresponding to an electron oscillation along the short axis of the rod, at around 510–550 nm for gold nanorods, and a longitudinal plasmon band, in the range 600–1200 nm.

Despite the appealing properties and tunability of gold nanorods (AuNRs) their seed-mediated synthesis relies on a complex and delicate equilibrium of reactants to achieve anisotropic growth conditions: silver ions and a surfactant agent (cetyltrimethylammonium bromide, CTAB) that shows preferential adsorption onto specific facets of gold and hinder reduction in these directions in presence of a weak enough reducing agent. A thorough understanding of the anisotropic growth mechanism and rigorous control over the synthetic parameters are required to guarantee reproducibility and fine-tune the optical properties of AuNRs. A great effort has been spent to elucidate the functions of the various reactants during growth, and consensus has been reached regarding the functions of the reducing agent, silver ions, seed, and CTAB. However, although it is well known that the presence of silver ions is required to increase the yield of AuNR synthesis and to regulate the aspect ratio, the role of silver as a shaping agent is still under debate. On one side it is reported the formation of metallic silver on the nanorods surface, suggesting a role of silver in directing the anisotropic growth by forming a sub-monolayer on selected AuNRs sidefacets, while other authors point out the lack of preferential absorption of silver on gold facets. Additionally, the presence of silver ions on the gold surface has been identified by other groups as well as the formation of a complex between CTAB and Ag(I). With the aim of elucidating the interaction between silver, CTAB and gold surface and to characterize the impact of silver and surfactant agents on the nanorods formation and growth, the local atomic structure around gold and silver were probed on two different kinds of CTAB stabilized gold nanorods. Different morphologies, aspect ratios and plasmon band positions were obtained using either Ascorbic Acid (AuNRs-AA) or Hydroquinone (AuNRs-HQ) as a reducing agent.

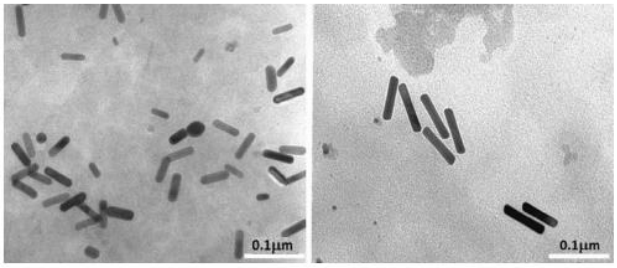

Figure 8: TEM images of: a)AuNRs-AA; b) AuNRs-HQ.

XAS measurements of Ag-K and Au-LIII edges were performed at ESRF and ELETTRA facilities respectively. Au LIII edge XANES show a close resemblance to those of the reference gold foil, with the characteristic “white line” of metallic gold (shoulder at 11920 eV), this is also confirmed by EXAFS analysis, where the bulk gold fcc structure was useful to fit contributions up to the fourth shell. Ag K edge XANES is very similar to that of Ag(I) model compounds with a feature at 25520 eV that is slightly less intense, indicating the presence of mostly ionic silver in the samples, with a minor contribution from metallic silver. EXAFS analysis of Ag-K edge confirms the presence of both types of silver, as well as its interactions with gold surface, other silver atoms and bromide ions from the above CTAB multilayer. In conclusion, combining XANES and EXAFS analysis (alongside complementary spectroscopic characterizations) on these systems indicated a gold-filled core that interacts of the surface with both metallic silver and Ag(I) ions, with possible Ag(I)-Br coordination. The fact that similar results were obtained for gold nanorods with different dimensions also implies that silver and its interactions with gold and CTAB, while being a key element to enforce anisotropic growth conditions, do not contribute majorly to the final size and aspect ratio of the nanorod obtained, which is mostly due to the choice of reducing agent.

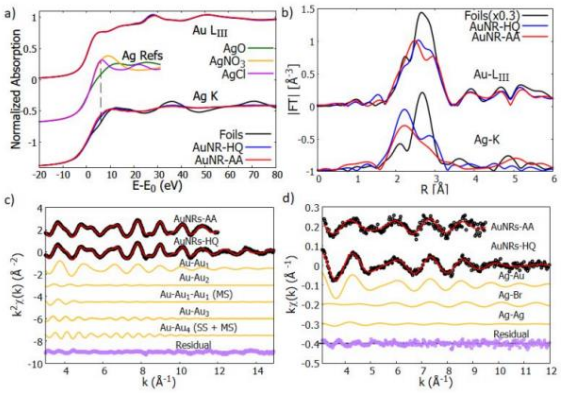

Figure 9: Normalized XANES spectra of Au-LIII (top curves) and AgK edge (bottom curves) measured on reference foils (Au and Ag, black lines) and on AuNR samples (AuNR-HQ: blue and AuNR-AA: red). The reference spectra of Ag+ (AgNO3 and AgCl) and Ag2+ (AgO) are shown for the sake of comparison. b) Moduli of the Fourier Transforms |FT| of kw weighted EXAFS spectra of Au-LIII (top curves) and Ag-K (bottom curves) edges for the reference foils (black lines) and AuNRs (AuNR-HQ: blue, AuNR-AA: red). c-d) Results of the Au-LIII/Ag-K edges EXAFS data fitting for AuNR-HQ and AuNR-AA samples. The experimental (black dots), best fit (red lines) and the partial contributions used for the analysis (orange lines) are shown (vertically shifted for clarity). The bottom curves (purple dots) represent the residues (experimental data minus best fit).

Pricipal Publication : S. Amatori, A. Lopez, C. Meneghini, A. Calcabrini, M. Colone, A. Stringaro, S. Migani, I. Khalakhan, G Iucci, I. Venditti and C. Battocchio; *Nanoscale Adv.*, 2023, 5, 3924-3933

Copper binding to cyanobacteria cells adopted as biosorbents: a structural study

M. Ciani[1], G.O. Lepore[2], S. Margheri[2], A. Puri[3], F. D'Acapito[3], A. Adessi[1]

[1]Department of Agriculture, Food, Environment and Forestry (DAGRI), University of Florence, [2]Department of Earth Sciences (DST), University of Florence, [3]CNR-IOM-OGG c/o ESRF – The European Synchrotron, Grenoble.

Cyanobacteria are photoautotrophic prokaryotes able to withstand different environmental conditions. The exopolysaccharides (EPS) covering cyanobacteria cells and the polysaccharides released in the surrounding medium (RPS) are characterized by a strong anionic character due to the presence of one or two different uronic acids as well as sulfate, carboxylic, and phosphate groups, representing chelating agents for positively charged HM [1,2]. Since the binding of the metal may be affected by the cyanobacteria strain, cellular fraction, metal type, and the simultaneous presence of more than one metal, several samples, treated with Ni, Cu and Zn solutions, were analyzed at the BM-08 LISA beamline, aiming at shedding light on the binding mechanisms and characterize the metal-organic materials obtained through biosorption process.

As an example, here, we present preliminary results on Cu binding to the cells of *Cyanothece* sp. CE4, a halophilic cyanobacterium characterized by a high content of uronic acids. The cells, previously kept in contact with a Cu^{2+}-solution and then freeze-dried (Figure 1, upper left), were able to remove 0.1 mmol Cu per gram of dry weight, corresponding to 0.3 mmol Cu per gram of total carbohydrates.

XAS investigation at Cu K-edge (8978.9 eV) was performed in the first experimental hutch (EH1) of BM-08 LISA beamline adopting a non-focused beam (1mmx2mm ca) and Si(311) monochromator crystals. The estimated flux on the sample was ~ $8*10^9$ ph/s. In order to reduce the possibility of beam damage, measurements were performed in vacuum at 80 K using a cold finger LN_2 cryostat. XAS spectra on the sample were acquired in fluorescence mode with a Si photodiode or in transmission mode for reference compounds, under vacuum conditions. Spectra of the samples were acquired with an energy increment of 1, 0.5, 0.15 eV in the pre-edge regions, with a constant increment of 0.5 eV in the edge region, and 0.05 eV in the post-edge region up to a maximum k value of 16 $Å^{-1}$.

ATHENA software was used for background removal, edge step normalization, energy calibration, and averaging of multiple spectra. Normalised XANES spectra of the sample and the reference compounds were compared to estimate the oxidation state of Cu and structural EXAFS signals ($k\cdot\chi(k)$) were extracted.

Fits were performed fixing the amplitude reduction factor (S_0^2) to the value obtained through the fit of $CuCl_2$, CuS, and CuO adopted as reference compounds. The first coordination shell around Cu was investigated by adopting mixed O/Cl path through ARTEMIS software The coordination number was defined following the bond valence model [3], thus considering the relationship between bond length, bond valence and coordination. As shown in *Figure 10* (upper right), the edge position in the sample, in comparison with the edge position of the reference compounds, indicates that Cu is still present as Cu^{2+}. The results of the fit (*Figure 10*, below) show that Cu is bonded to both Cl and O with Cu-Cl and Cu-O distances resulted of 2.23 ± 0.03 Å and 1.92 ± 0.06 Å and a coordination number with Cl and O of 2.9 and 0.9, respectively.

Since EXAFS cannot discriminate among atoms with similar Z, the presence of N and C instead of (or mixed with) O and of P and S instead of (or mixed with) Cl cannot be excluded. All these elements are commonly found in cyanobacterial biomass.

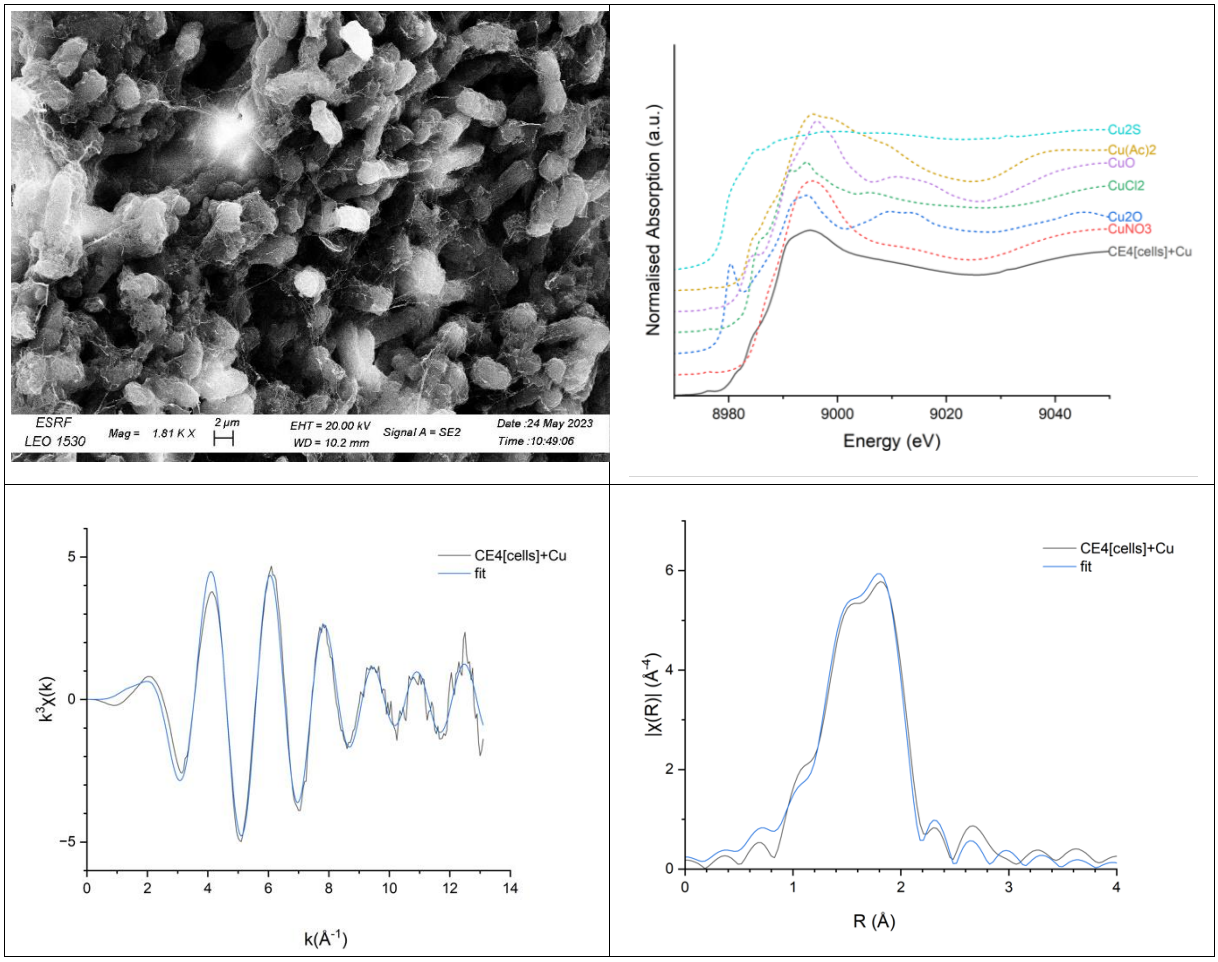

*Figure 10: A**bove**: SEM micrographs (1800x magnitude) of CE4[cells]+Cu sample (left). Normalised XANES spectra of CE4[cells]+Cu sample (black line) and selected model compounds (dashed lines) (right). **Below**: Cu K-edge k^3-weighted EXAFS region (left) and Fourier transforms (right) of CE4[cells]+Cu sample, black lines are data, blue lines are fits. Energy was calibrated with a Cu reference foil (8978.9 eV).*

Further analyses are currently ongoing on other Cu-Zn-Ni-treated samples, comparing the two cellular fractions and the two cyanobacteria strains. The comparison of the XAS results coupled with the information obtained by other techniques such as SEM, TEM, chromatography and FT-IR spectroscopy, will be necessary to clarify the binding mechanisms of heavy metals to cyanobacteria.

References:

[1] M. Ciani and A. Adessi, *Frontiers in Microbiology*, vol. 14, 2023,

[2] C. Laroche, *Marine Drugs*, vol. 20, no. 5, Art. no. 5, 2022

[3] I. D. Brown and D. Altermatt, *Acta Cryst B*, vol. 41, no. 4, pp. 244–247. 1985

Temperature dependent EXAFS spectroscopy on silica coated Fe-triazole nanoparticles

E. Petsali [1], F. Pinakidou[2], V. Tangoulis[2], N. Lalioti[2], F. D'Acapito[3],E. C. Paloura[1], A. Puri,[3]M. Katsikini[1]
[1]Aristotle University of Thessaloniki, School of Physics, Dept. of Cond. Matter and Mat. Physics, 54124 Thessaloniki, Greece,
[2] University of Patras, Department of Chemistry, Laboratory of Inorganic Chemistry, 26504 Patras, Greece
[3]CNR-IOM-OGG, c/o ESRF LISA CRG, Avenue des Martyrs 71, 38000 Grenoble, France

In the rapidly evolving field of materials science, the concept of molecular switches has garnered significant interest due to their potential applications in various domains, including memory storage, sensors, medicine, and smart materials. Central to this interest is the unique ability of these switches to alternate between distinct states in response to external stimuli, such as temperature, light, or magnetic fields.

One compelling example of molecular switches is found in the iron(II)-triazole complexes, which exhibit the spin crossover (SCO) phenomenon. This remarkable trait allows them to exist in two distinct spin states: a low-spin (LS) state and a high-spin (HS) state. The low-spin state is characterized by a smaller ionic radius and lower magnetic moment, while the high-spin state exhibits a larger ionic radius and higher magnetic moment. The transition between these states is reversible and can be triggered by changes in environmental conditions, such as temperature, making them ideal candidates for studying and harnessing the potential of molecular switches.

The focus of this research lies on the investigation of these transitions in Fe-triazole nanoparticles along with the impact of sample preparation on the spin-state transition. By employing temperature-dependent EXAFS spectroscopy, a powerful technique for probing the local structure and electronic properties of materials, this research aims to elucidate the intricate details of the spin crossover transition in these nanoparticles. Understanding these transitions at a molecular level is crucial for the development of advanced materials that can effectively respond to external stimuli, paving the way for innovative applications in the field of smart materials and beyond.

The Fe-Trz nanoparticles were synthesized by employing a reverse micelle technique and the Fe-K-edge EXAFS measurements were conducted at the LISA beamline (BM08). The spectra were recorded in the temperature range 80 - 485 K using a liquid nitrogen cryostat. Figure 11(a) shows the spectrum of Fe-Trz nanoparticles coated with silica in the R-space and the corresponding fitting. Fe was found octahedrally coordinated with N atoms belonging to the Trz ligands. At distances 3-5 Å, strong multiple scattering contribution is observed originating from bonding of Fe with the planar triazole ring. Furthermore, a peak that appeared at approximately 7 Å, is attributed to Fe-Fe-Fe multiple scattering events and is indicative of the chain polymerization.

Fourier Transform (FT) amplitudes of the spectra recorded upon heating and subsequent cooling are shown in Figure 11(b). Upon temperature increase, a splitting in the first nearest neighbouring shell is observed at T≥470 K. Two different Fe-N distances were identified at approximately 1.96 and 2.15 Å, corresponding to the LS and HS state of Fe. During temperature decrease, a pure LS state occurs at 350 K indicating a hysteresis in the HS to LS transition. The overall results demonstrated that the pressure applied during pellet formation and the thermal treatment under high vacuum prior to spectra acquisition influence the temperature at which the LS to HS transition initiates. Finally, the temperature dependence of the Debye-Waller Factor (DWF) in the first nearest neighbouring shell (Fe-N) was studied in the case of a sample that was not subjected to thermal treatment where the LS to HS transition did not occur. Using the Einstein model to fit the DWF vs temperature

dependence, an Einstein temperature equal to 550 K for the Fe-N first nearest neighbour interaction was determined.

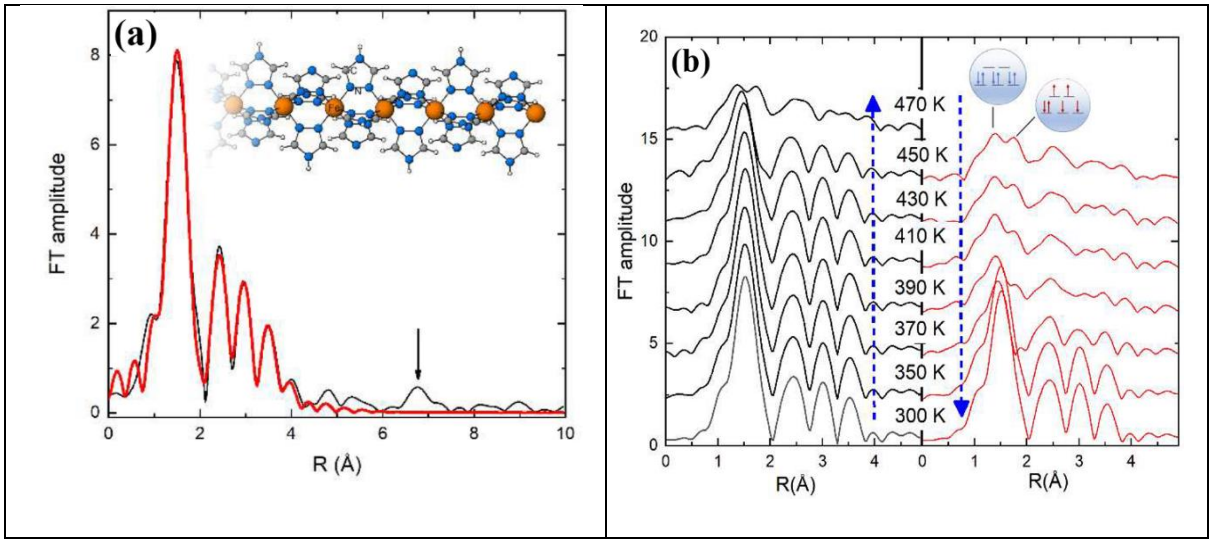

Figure 11: *(a) FT amplitude of the EXAFS χ(k) spectrum recorded at room temperature. Black and red lines correspond to the experimental and fitting curves, respectively. (b) FT amplitude of the EXAFS χ(k) spectra recorded at 300K to 470 K (heating and cooling).*

X-Ray Absorption Spectroscopy as a tool for studying molybdenum recovery from solid waste

R.E Russo [1], M. Fattobene [1], S. Zamponi [1], M. Berrettoni [1], G. Giuli [1] and F. d'Acapito [2]

[1]School of Science and Technology, University of Camerino – ChIP buildings, Camerino, 62032 Italy
[2]CNR-Istituto Officina dei Materiali (IOM)-OGG, c/o ESRF-71, Avenue des Martyrs, 38043 Grenoble, France

Molybdenum finds applications in many industrial and chemical sectors, such as steel production, lubricants, electrical components, and catalysts. It is not classified as a critical raw material by the European Commission in 2023 but it could be considered potentially critical because of its position on the borderline between non-critical raw materials and the criticality zone, underscored by a notably high supply risk score of 0.8. In this research, a sustainable and eco-friendly hydrometallurgical approach is employed to recover molybdenum from spent oxidation catalyst used in formaldehyde production. The method utilizes a soft green acid derived from agri-food waste by-products, specifically tartaric acid obtained from winery waste, used as both a leaching and chelating agent.[1]
Commercially iron molybdate catalyst always contain $Fe_2(MoO_4)_3$ and MoO_3, with a tetrahedral and distorted octahedral geometry, respectively.[2] XRD patter exhibits two large peaks corresponding to amorphous phase and, mainly, can be identified the peaks of $Fe_2(MoO_4)_3$ and MoO_3. X-Ray absorption spectroscopy (XAS) can confirm the phases identification in the amorphous matrix, the exact oxidation state in the sample and his chemical environment. These data are important for understanding and investigating a better leaching process, including decisions such as whether the addition of an oxidizing agent is required.
XAS investigation at Mo K-edges of a spent catalyst was carried out using a Si(111) double-crystal monochromator and collecting data in transmission mode. Single point XAS spectra was recorded in transmission mode with a beam with sizes (h×v) of ~ 4x1.5 mm. The Mo K-XANES spectra (Figure #a) exhibit a pre-edge peak at ~20.004 eV. It is attributed to the dipole-forbidden/quadrupole-allowed 1s–4d transition, which is associated primarily with tetrahedral geometry. In fact, there is a significantly larger pre-edge peak observed for $Fe_2(MoO_4)_3$ compared to MoO_3, where the same characteristic is present but to a lesser degree.[3] Qualitatively, XANES of spent catalyst appear more similar to $Fe_2(MoO_4)_3$ than MoO_3 (Figure 12 A).

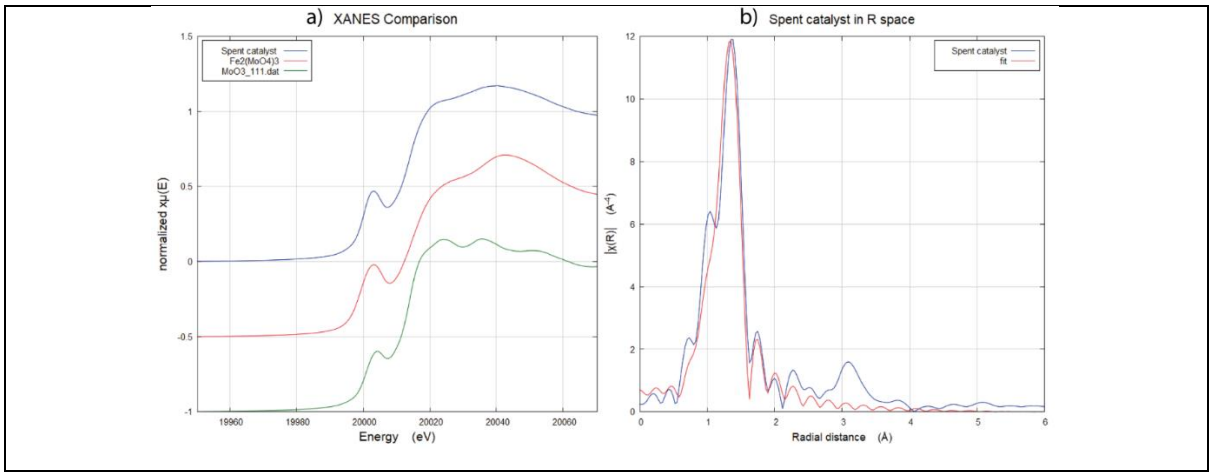

Figure 12 a) Xanes comparison of spent catalyst in blue, $Fe_2(MoO_4)_3$ in red and MoO_3 in green. Region from -50 to 70; b) Fitting (in red) between spent catalyst and the first shell of $Fe_2(MoO_4)_3$.

EXAFS spectroscopy investigation was performed trying to fit both phases. A bad fitting values was obtained with the first shell of MoO_3. While a good fitting was obtained with the first shell Mo-O of $Fe_2(MoO_4)_3$ (Figure 12 B) showed the following values (uncertainties in parentheses): R(Å) 1.75(0.01); σ^2(Å^2) 0.004(0.001), N=4 (fixed).
In summary, the XAS analysis leads to the conclusion that molybdenum primarily exists in the +6 oxidation state. Furthermore, the presence of $Fe_2(MoO_4)_3$ can be confirmed through XANES and EXAFS fitting, although a more comprehensive shell analysis beyond one would be required. Conversely, there is a possibility that MoO_3 may be present in trace amounts.

References

1. Russo R.E, Ventura M, Fattobene M, et al. Hydrometallurgical Molybdenum Recovery from Spent Catalyst Using Tartaric Acid Derived from Agrifood Waste. *ACS Sustain Chem Eng*. 2023;11(43):15644-15650. doi:10.1021/acssuschemeng.3c04318
2. Malik MI, Abatzoglou N, Achouri IE. Methanol to formaldehyde: An overview of surface studies and performance of an iron molybdate catalyst. *Catalysts*. 2021;11(8). doi:10.3390/catal11080893
3. Gaur A, Stehle M, Raun KV, et al. Structural dynamics of an iron molybdate catalyst under redox cycling conditions studied with: In situ multi edge XAS and XRD. *Physical Chemistry Chemical Physics*. 2020;22(20):11713-11723. doi:10.1039/d0cp01506g

Sequestration of Zinc in pyrochlores: a XAS analysis

S. Margheri[1], M. Goudjil[1], A. Puri[2], I. Orsilli[3], P. Bonazzi[1], L. Bindi[1], F. d'Acapito[2] and G.O. Lepore[1]
[1]Dipartimento di Scienze della Terra (DST), Università degli Studi di Firenze (Unifi), via La Pira 4, 50121 Firenze, Italy,
[2]CNR-Istituto Officina dei Materiali (IOM)-OGG, c/o ESRF-71, Avenue des Martyrs, 38043 Grenoble, France,
[3]Dipartimento di Scienze dei Materiali, Università degli studi di Milano-Bicocca (Unimib), 210125 Milano, Italy.

The crystal structure of pyrochlores ($A_xB_2O_6Y$) is characterized by a framework of corner sharing BO_6 octahedra, (where B is generally a high-field strength elements such as Nb or Ta) which describe an interweaving of tunnels that can be occupied by a wide range of ions (like K^+, Na^+, Ca^{2+}, OH^-) and water molecules. [1,2] The tunnel ions are distributed in two distinct crystallographic sites A and Y. Nevertheless, they can be displaced from A and Y positions to a constellation of surrounding sites. Moreover, the ions in the tunnels are quite mobile and can be exchanged with the external environment.[3]
The purpose of the experiments conducted at BM08 LISA beamline is to investigate the ability of pyrochlores to incorporate Zn within the tunnels of their crystal structure.
These experiments are part of a PhD project, aimed at investigating the ion exchange properties of pyrochlores for the removal and recovery of heavy metals from polluted waters and industrial wastewaters. XAS investigations are necessary to study the incorporation mechanisms of pyrochlores, the environment around the tunnel sites and the eventual variations in the crystal structure due to the ionic exchanges. Synthetic powders of KTa_2O_5OH and NaW_2O_6OH were first immerged in aqueous solutions on $Zn(NO_3)_2$ with concentrations of Zn ranging from 1 to 10^{-6} M. X-ray powder diffraction analysis (XRPD) where used to verify the purity of the powders before and after the treatment.
XAS investigations were conducted at Zn K-edge (9.659 KeV) and W, Ta L_3-edge (10.207and 9.881 KeV, respectively) in 4 bunches mode using a Si (111) double-crystal monochromator. Zn, Ta and W metal foils were used as standard for energy calibrations. A WO_3 pellet was used as a model compound to evaluate the oxidation state of W in the NaW_2O_6OH pyrochlore (Figure 13). From the edge position W in NaW_2O_6OH seems to have the same oxidation state of that in WO_3, which is 6+.

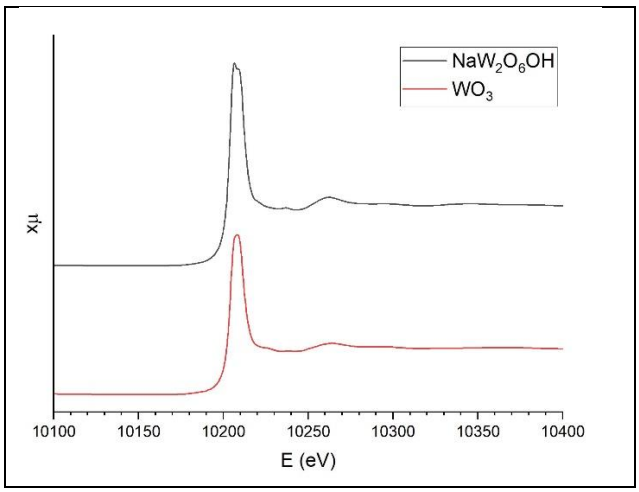

Figure 13 *L_3 W-edge of NaW_2O_6OH pyrochlore and WO_3 standard.*

Single point XAS spectra were collected in high vacuum condition with a temperature of 80 K, obtained using a cold finger LN2 cryostat. Spectral profiles were collected in both transmission and fluorescence mode. Ion chambers filled with Argon gas were used for

transmission data collections, while the fluorescence spectra were acquired using a 12 elements HpGe detector.
XAS data were processed using the Athena software, while Artemis will be used for the fitting. Data reduction and analysis is still ongoing.
XAS analyses will be supported by XRPD and Pair Distribution Function (PDF) experiments, already scheduled at ID11.

References

[1] Atencio D., Andrade M.B., Christy A.G., Gieré R. and Kartashov P.M. (2010). The pyrochlore supergroup of minerals: nomenclature. *The Canadian Mineralogist*, 48, 673-689.
[2] Atencio D. (2021). Pyrochlore-Supergroup minerals nomenclature: an update. *Frontiers in Chemistry, Solid State Chemistry*, 9, article 713368.
[3] Möller T., Clearfield A. and Harjula R. (2001). The effect of cell dimension of hydrous mixed metal oxides with a pyrochlore structure on the ion-exchange properties. *Chemistry of Materials*, 13, 4767-4772

Scientific Highlights

Total electron yield (TEY) detection mode Cr K-edge XANES spectroscopy as a direct method to probe the surface composition of darkened chromate-based yellow paints

*L. Monico,[1,2] * F. d'Acapito,[3] M.e Cotte,[4] K. Janssens,[2] A. Romani,[1] G. Ricci,[1] C. Miliani,[5] L. Cartechini[1]*
[1] CNR-SCITEC and Centre of Excellence SMAArt - Perugia University, Italy, [2] AXIS and NANOlab Centre of Excellence, University of Antwerp, Belgium [3] CNR-IOM-OGG, c/o ESRF LISA CRG, Grenoble, France. [4] ESRF, Grenoble, France.[5] CNR-ISPC, Napoli, Italy.

The past few decades have seen a remarkable increase in the use of synchrotron radiation (SR)-based X-ray methods with micro-/nano-beams to study the color changes due to chemical alteration of pigments in paintings. Micro-X-ray near edge structure (μ-XANES) spectroscopy in X-ray fluorescence yield detection mode (XFY) was often employed to perform non-destructive stratigraphic elemental speciation analysis of non-transparent samples down to the (sub)micrometre scale length. [i] Nevertheless, preparation of samples as cross sections is demanding and time consuming with the composition of the analyzed micro-samples that might be not fully representative of the studied phenomena. [ii]

In this scenario, it becomes significant to explore how SR-based X-ray methods may permit to obtain direct surface elemental speciation information from larger, non-transparent and layered fragments, while reducing lengthy sample preparation procedures. Total electron yield (TEY) detection mode has been proved to be a suitable alternative to indirect XAS analysis in XFY mode to study selectively the surface of different kind of artworks due to the shallowness of the electron escape depth (of the order of tens of nm) compared with X-ray fluorescence. [iii]

In the present study, we have systematically explored the capabilities of Cr K-edge XANES spectroscopy collected at the same time in XFY and TEY detection modes to perform Cr speciation investigations of the darkened surface of a set of chromate-based yellow oil paints made up of either the sulfate-rich chrome yellow type ($PbCr_{0.2}S_{0.8}O_4$; denoted as $Cr_{0.2}Y$) or potassium chromate (K_2CrO_4). Both class of compounds undergo darkening due to a reduction of the original Cr^{VI} to Cr^{III}-compounds, with Cr^{V}-species arising from the interaction between the pigment and the oily binder. The process, that usually involves the uppermost 5-10 micrometres of the paint stratigraphy, has been found as the cause of darkening of several paintings by Vincent van Gogh. [iv]

Figure 14 shows the Cr-K edge XANES spectra collected at the same time in XFY and TEY detection modes at BM08 beamline from surface of paint fragments. Data reveal that only Cr^{VI} compounds are present in samples unaged-$Cr_{0.2}Y$ and 0 days-K_2CrO_4 (Figure 14 C, D red lines), as highlighted by the intense pre-edge peak at 5.993 keV. In both aged paints (Figure 14 C, D, black and grey lines), the partial conversion of Cr^{VI} to Cr^{III}-compounds is pointed out by the decreasing of the pre-edge peak intensity and by a shift of the absorption edge energy. Nevertheless, the contribution of reduced Cr-species is higher in the spectrum recorded in TEY mode than XFY mode, as shown by a more significant decrease of the pre-edge peak intensity (see inset) and shift of the absorption edge towards lower energy along with a loss of structure of the post-absorption features. This result can be explained considering the lower sampling depth of TEY mode measurements with respect to XFY mode ones, that, under the employed experimental conditions, allows the composition of the superficial brownish layer to be probed selectively. This hypothesis is also further supported by the similarities shown with XFY mode μ-XANES spectra recorded at ID21 beamline from the uppermost darkened layer of thin sections prepared from the same set of paints (data not shown).

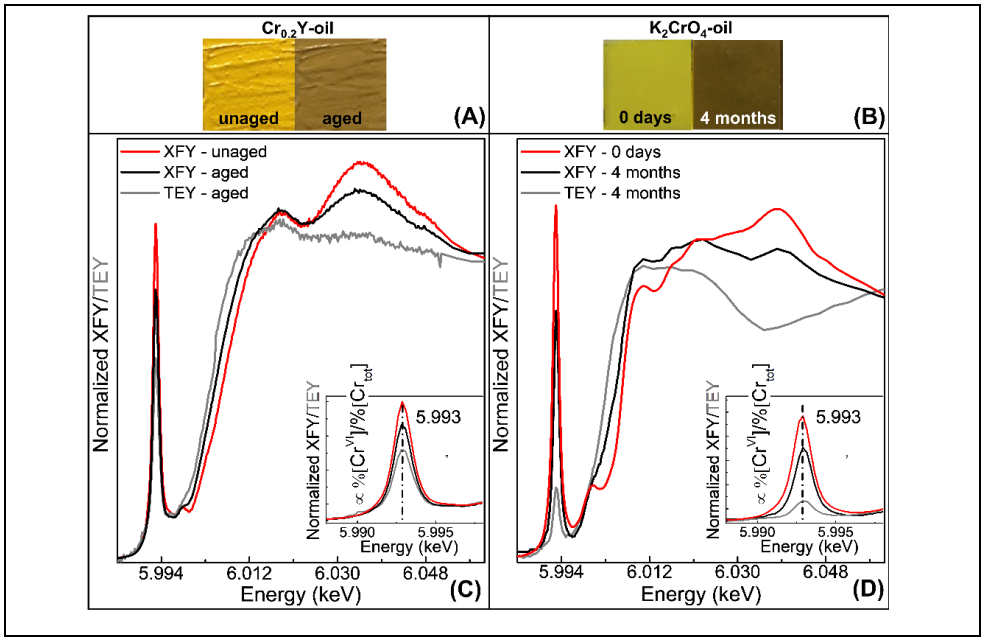

Figure 14. Photographs of oil paint mock-ups made up of (A) $Cr_{0.2}Y$ ($PbCr_{0.2}S_{0.8}O_4$) before (left)and after esposure to light and (B) K_2CrO_4 collected immediately (0 days) and 4 months after preparation of the sample. (C) Cr K-edge XANES spectra collected from (C) $Cr_{0.2}Y$ and (D) K_2CrO_4 oil paint mock-ups in XFY mode (red, black lines) and TEY mode (grey) at BM08.

Overall, TEY-XANES spectroscopy can be profitably employed as a primary approach to study the composition of surface of sample on the sub-millimetric scale length, thus driving, in a subsequent step, the preparation of sectioned samples and relative studies at the submicrometric scale length by µ-XANES spectroscopy in XFY mode. Furthermore, the outcomes of this study open further research into the application of such combined TEY-XANES/XFY µ-XANES methodological approach also to the study of the degradation pathways of other pigments in fragments from artificially aged paint mock-ups and different kinds of unvarnished historical painted objects.

References

[1] K. Janssens, M. Cotte, Using Synchrotron Radiation for Characterization of Cultural Heritage Materials. In: E. Jaeschke, S. Khan, J. Schneider, J. Hastings (eds), Synchrotron Light Sources and Free-Electron Lasers. Springer, Cham. (2020), pp. 2457–2483, https://doi.org/10.1007/978-3-030-23201-6_78.

[1] E. Pouyet, B. Fayard, M. Salomé, Y. Taniguchi, F. Sette, M. Cotte, *Heritage Sci.*, 3 (2015), 1-16, https://doi.org/10.1186/s40494-014-0030-1.

[1] N. Isomura, K. Oh-Ishi, N. Takahashi, S. Kosaka, *J. Synchrotron Rad.*, 28 (2021), 1820-1824, https://doi.org/10.1107/S1600577521009401.

[1] L. Monico, K. Janssens, E. Hendriks, F. Vanmeert, G. Van der Snickt, M. Cotte, G. Falkenberg, B. G. Brunetti, C. Miliani, *Angew. Chem., Int. Ed. Engl.*, 54 (2015), 13923-13927, https://doi.org/10.1002/anie.201505840.

Publication: [Nucl. Instrum. Methods Phys. Res., Sect. B 539 (2023), 141]

Giant uniaxial negative thermal expansion in $FeZr_2$ alloy over a wide temperature range

M. Xu[1], Q. Li[2], Y. Song[1], Y. Xu[3], A. Sanson[4,5], N. Shi[1], N. Wang[1], Q. Sun[6], C. Wang[1], X. Chen[2], Y. Qiao[6], F. Long[1], H. Liu[1], Q. Zhang[7], A. Venier[4], Y. Ren[8], F. d'Acapito[9], L. Olivi[10], D. O. De Souza[10], X. Xing[2], Jun Chen[1,11]

[1]Beijing Advanced Innovation Center for Materials Genome Engineering, Department of Physical Chemistry, University of Science and Technology Beijing, China. [2]Institute of Solid State Chemistry, University of Science and Technology Beijing, China. [3]Institute for Applied Physics, University of Science and Technology Beijing, China. [4]Department of Physics and Astronomy, University of Padua, Italy. [5]Department of Management and Engineering, University of Padua, Italy. [6]International Laboratory for Quantum Functional Materials of Henan, Zhengzhou University, China. [7]Neutron Scattering Division, Oak Ridge National Laboratory, USA. [8]Department of Physics, City University of Hong Kong, China. [9]CNR-IOM-OGG c/o European Synchrotron Radiation Facility (ESRF), Grenoble, France. [10]ELETTRA Synchrotron Trieste, Italy. [11]Hainan University, China.

Negative thermal expansion (NTE), which is the contraction of volume upon heating, is an unusual property of materials. Over the last two decades, NTE has garnered significant attention for its potential to produce materials with controlled thermal expansion - a critical factor in various engineering and technological applications requiring thermal stability. Examples include precise instruments, aerospace materials, micromechanics, as well as photonic and electronic devices. Since then, numerous NTE materials have been discovered, and various NTE mechanisms have been investigated. NTE over a wide temperature range is indeed the key element enabling the development of materials with controlled thermal expansion. In this study, we have identified a giant uniaxial NTE in $FeZr_2$ alloy across a broad temperature range (α_l = -34.0x10^{-6} K^{-1} from 93 K to 1078 K), representing the largest NTE observed among all metal-based materials to date, with $\Delta L/L = -3.35\%$.
To elucidate the NTE mechanism of the $FeZr_2$ alloy, we conducted a study on its structure and vibrational dynamics using XAFS spectroscopy, neutron and X-ray diffraction, combined with first-principles calculations. A comparative analysis was also undertaken with the isostructural $NiZr_2$ alloy, which exhibits positive thermal expansion.

Table 1: Bond effective force constants determined by EXAFS.

Sample	$K_{\parallel}$ (eV/Å²) Zr-M	$K_{\parallel}$ (eV/Å²) M-M	$K_{\perp}$ (eV/Å²) Zr-M
$FeZr_2$	2.76 ± 0.03	2.36 ± 0.26	0.40 ± 0.02
$NiZr_2$	3.78 ± 0.10	3.61 ± 0.28	1.12 ± 0.35

It is well known that NTE mechanism in alloys is generally related to magnetic-volume effect, phase transition or charge transfer. However, diffraction shows no magnetic or phase transition in $FeZr_2$, and Fe and Zr K-edges XANES do not reveal any charge transfer. Therefore, we can guess that the NTE is related to the framework structure of $FeZr_2$ and the corresponding lattice dynamics. As confirmation of this, first-principles calculations in $FeZr_2$ reveal a large presence of vibrational modes with a negative Grüneisen parameter, unlike the modes in $NiZr_2$, which are mostly positive. Interestingly, the negative Grüneisen parameters in $FeZr_2$ are more pronounced and prevalent in the optical modes region than in the acoustic region. To provide a more comprehensive explanation of the NTE behaviour, the study of vibrational dynamics through EXAFS spectroscopy becomes fundamental. Table 1 displays the bond effective force constants determined by EXAFS for the Zr–M and M–M bonds: they decrease from $NiZr_2$ to $FeZr_2$, indicating that the Fe_2Zr_4 octahedra are composed of relatively soft Zr–Fe and Fe–Fe bonds. Figure 15 a-b shows the temperature dependence of the "true" and "apparent" bond expansion measured by EXAFS and diffraction, respectively. The difference between them is associated with the presence of transverse atomic vibrations,

which is strongly correlated with NTE. The expansion of the Zr–Fe bond is significantly larger than that of the Zr–Ni bond, suggesting that the relatively weak strength of the Zr–Fe bond imposes less constraint on the Fe_2Zr_4 octahedra. Due to the large expansion of the Zr–Fe bond, the Fe–Fe bond, which has relatively weak strength, contracts to maintain the stability of the Fe_2Zr_4 octahedra. This results in a large shrinkage along the c-axis (Figure 15 c). Conversely, the stiffer bonds in the Ni_2Zr_4 octahedra lead to normal positive thermal expansion in $NiZr_2$ (Figure 15 d).

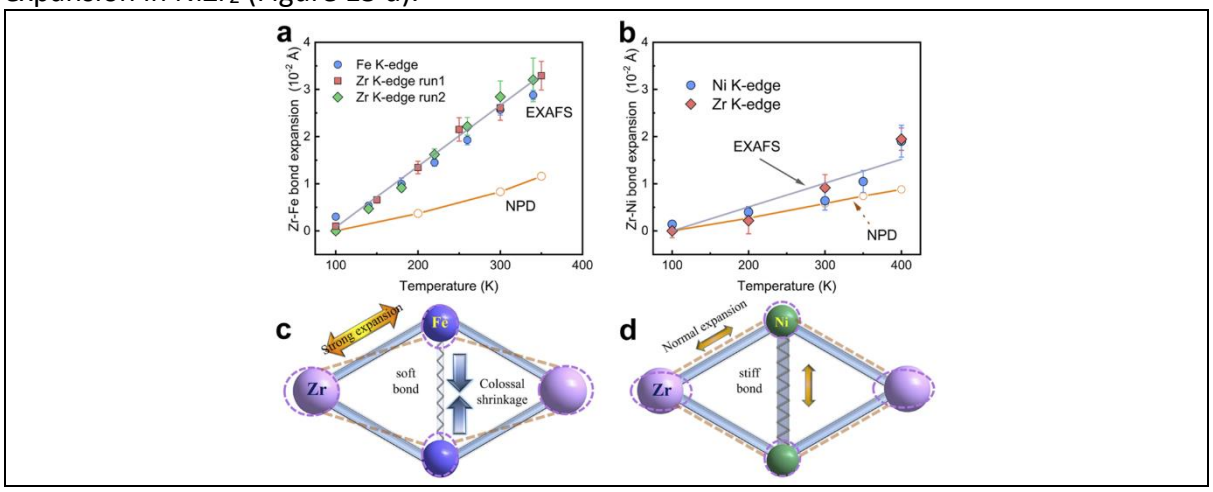

Figure 15: Schematic diagram illustrating the giant 1D negative thermal expansion of $FeZr_2$. Panels (a) and (b) display the Zr–M (M = Fe, Ni) bond expansion in $FeZr_2$ and $NiZr_2$, respectively. The true bond expansion, extracted by EXAFS, is depicted as the gray lines with symbols, while the apparent bond expansion measured by diffraction is represented by the orange lines with symbols. Panels (c) and (d) illustrate the mechanism of giant 1D NTE in $FeZr_2$ and the comparison with $NiZr_2$, respectively

In other words, the giant 1D NTE observed in metallic $FeZr_2$ originates from phonon vibrations driven by the flexible structure of $FeZr_2$. To conclude, the present work reports a giant uniaxial NTE over a wide temperature range in metallic $FeZr_2$, which is the largest observed among metal-based materials. This NTE is phonon-induced by the flexible structure, although phonon-induced NTE is rare in metal-based materials. This study provides a new direction for developing NTE materials and controlling thermal expansion.

Publication: [Nature Comm. 14 (2023), 4439].

High-entropy alloys investigated by extended X-ray absorption fine structure

A. Fantin[1,2]
[1]Bundesanstalt für Materialforschung und -prüfung (BAM), [2]Helmholtz-Zentrum Berlin (HZB)

Complex multi-component alloys, also known as High-Entropy Alloys (HEA), originate from the high configurational entropy *S* that, by overcoming the enthalpy of formation *H*, decreases the overall systems' Gibbs Energy *G* (*G* = *H*-*TS*, with *T* temperature) thus stabilizing the alloy crystal structure. As the mechanical performances are generally dependent on the atomic synergies within the solid solution phase but also between the solid solution and eventual segregated intermetallic phases, studies at the atomic level including site preferences, chemical ordering and local lattice distortions are crucial. Extended X-ray absorption spectroscopy (EXAFS) is a powerful technique in this scenario and allowed investigations both on i) the solid solution of twelve *fcc*-based Medium-Entropy ternary to High-Entropy senary alloys and ii) the topologically-close packed (TCP) σ-phase, one of the best-known and most widely studied intermetallic phase. Both the TCP-σ and *fcc* systems are based on 3*d* metals, whose EXAFS measurements at K-edges were collected at LISA-BM08 beamline (CRG-ESRF).

How atomic bonding plays the hardness behavior in the Al-Co-Cr-Cu-Fe-Ni high entropy family

A. Fantin[1,2], G.O. Lepore[3], M. Widom[4], S. Kasatikov[2], A. M. Manzoni

[1]BAM, [2]HZB, [3]University of Florence, [4]Carnegie Mellon University

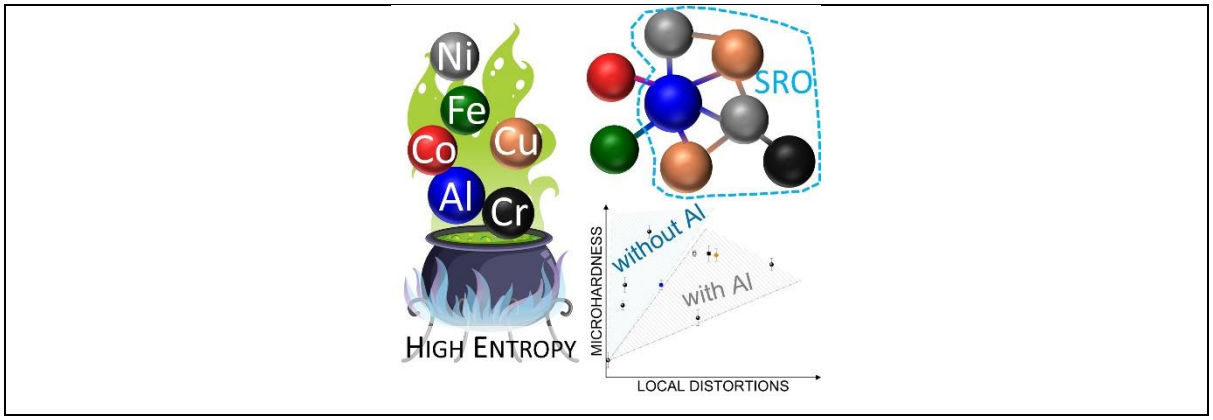

Figure 16: Graphical abstract (from ref. 1) evidencing the high-entropy alloy concept, the presence of specific short-range order (SRO), and the microhardness-to-distortions relationship

A systematic study carried out on the senary high-entropy $Al_8Co_{17}Cr_{17}Cu_8Fe_{17}Ni_{33}$ alloy and its quinaries, quaternaries and ternaries sub-alloys, demonstrates how specific element removal influences the material on both atomic-scale and macroscopic levels. Local distortions, by EXAFS analysis, and variations in the electronic structure, by XANES analysis, were related to material performance such as microhardness, highlighting the correlation of some effects in HEAs, i.e., "baseless" system with no predominating elements, to the intrinsic nature of the solid solution. Specific interest was addressed to the comparison between the senary $Al_8Co_{17}Cr_{17}Cu_8Fe_{17}Ni_{33}$ and five quinaries obtained by removing one element at a time, keeping the elemental ratio constant. Chemical short-range order at the 1st shell was determined through EXAFS analysis, showing the preferences of Al for Ni/Cu, which was corroborated by Monte Carlo/molecular dynamics simulations. Another discussed aspect is the appearance in the quinary alloys of a secondary ordered phase when Fe, or Co,

was removed from the senary alloy, hinting that both elements “hold together” the alloy solid solution.

Site occupancies in a chemically complex σ -phase from the high-entropy Cr-Mn-Fe-Co-Ni system

J.M. Joubert[1], Y. Kalchev[2], A. Fantin[3,4],J.-C. Crivello[1], R. Zehl[2], E. Elkaim[5], G. Laplanche[2]

[1]ICMPE, RU Bochum[2], TU Berlin[3], HZB[4], SOLEIL[5]

The σ-phase is extremely hard and brittle and, therefore, does not easily allow for conventional mm-size specimen preparation for macroscopic mechanical characterizations, which would benefit the understanding of why the σ-phase precipitation embrittles engineering alloys and hinders their corrosion resistance. Density functional theory (DFT) calculations could assist in resolving this obstacle if, however, precise crystallographic information is provided. By using the complementarity of resonant diffraction, DFT and EXAFS analysis, the crystal structure of a 5-component σ-phase was accurately determined, allowing to resolve the $P4_2/mnm$ space group with 30 atoms per unit cell, five different Wyckoff sites (2*a*, 4*f*, 8i_1, 8i_2, 8*j*) with different coordination numbers (CN). Resonant synchrotron diffraction experiments in the vicinity of the K-edges allowed determining the site occupancy through Rietveld refinement (Figure 17 left), which was used as input for EXAFS data modelling (Figure 17 right). Notice the good agreement between the elements which prefer site with larger CN (therefore longer distances) such as Cr, opposed to elements preferring sites with lower coordination numbers (shorter distances) such as Co or Ni.

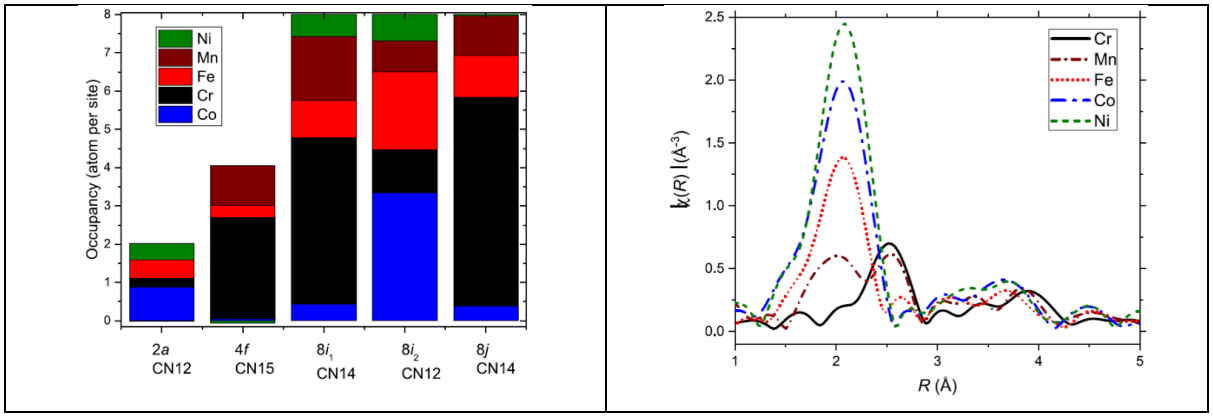

Figure 17: [readjusted from ref. 2 with permission of Elsevier]: ***Left****: site occupancies of Cr, Mn, Fe, Co and Ni on the five different sublattices of the quinary σ-phase obtained experimentally from the resonant diffraction experiment (f’ values from Sasaki)* ***Right****: χ(R) from EXAFS data acquired at LISA-BM08, of Cr, Mn, Fe, Co and Ni in the σ-phase, highlighting the different local-environments of each element.*

Publications: Small Sci. (2023), 2300225. Acta Mat. 259 (2023), 119277.

A laser synthesis route to boron-doped gold nanoparticles designed for X-ray radiotherapy and boron neutron capture therapy assisted by CT imaging

S. Scaramuzza,[1] C. M.G. de Faria,[1] V. Coviello,[1] D. Forrer,[1,2] L. Artiglia,[1] D. Badocco,[1] P. Pastore,[1] P. Ghigna,[3] I. Postuma,[4] S. Bortolussi,[3,4] R. Vago,[5] A. E. Spinelli,[5] M. Bekić,[6] M. Ĉolić,[6,7] V. Amendola[1]
[1]University of Padova, [2]CNR – ICMATE, [3]University of Pavia, [4]INFN-Pavia [5]IRCCS San Raffaele Scientific Institute, [6]University of Belgrade, [7]University of East Sarajevo

Nanomedicine, *i.e.* the applications of nanotechnology to medicine, has provided the possibility of delivering drugs to specific cells using the nanoparticles. The overall drug consumption and side-effects may be lowered significantly by depositing the active pharmaceutical agent in the morbid region only and in no higher dose than needed. Targeted drug delivery is intended to reduce the side effects of drugs with concomitant decreases in consumption and treatment expenses.
A key aspect for the progress of these aspects of nanomedicine is the continuous exploration of the multiple possibilities available by the combination of inorganic, organic and biological nanostructured components aiming to the improvement of medical technologies. In this context, the nanoalloys are in the spotlight as powerful and versatile materials for the integration of various functionalities in a single nanomedicine.
Radiotherapy and radiodiagnostic are fields where nanoalloys can enable unprecedented possibilities by the development of sensitizers for complementary radiation types. This is even more advantageous if the nanoparticles are tailored for therapy guidance with well-established tomographic imaging techniques such as MRI, CT or PET/SPECT. For instance, Fe-B NPs combine the radiosensitization ability for boron neutron capture therapy (BNCT) with MRI and interesting magnetic properties for magnetophoretic accumulation in tissues and magnetic hyperthermia.
In this work, we developed a new Au-B alloy as a multifunctional theranostic nanovector for the combination of BNCT and X-ray radio-therapy (XRT), with the support of CT for the localization and quantification of the radiosensitizers in tissues, which is a crucial aspect for BNCT. The Au-B NPs were obtained from a laser ablation in liquid process and subsequently coated with biocompatible polymers as DEX or thiolated PEG. The laser-assisted synthetic pathway granted reproducibility, environmental sustainability, and cost affordability, as required for scale-up of the production route. The structural features of Au-B NPs were identified, demonstrating the coexistence of the two elements in the NPs and explaining it with the support of DFT calculations, which is an absolutely novelty in the panorama of nanotechnology. The Au-B NPs have a marked gold character (see Figure 18), including the advantageous surface chemistry with thiolated compounds, biocompatibility and stability, and proved to act as radiosensitizers for both BNCT and XRT, as well as allowing the localization and quantification by CT imaging. A five-fold empowering of BNCT performances is straightforward by using a ^{10}B enriched composition. Overall, the Au-B NPs have the optimal features for the investigation of combined BNCT and XRT, supported by computed tomography (CT) imaging and with the straightforward integration of surface agents for cell targeting and internalization, which are crucial for appropriate intracellular localization. By this Au-B nanotheranostic tool, it is now possible to shed light on scarcely investigated or completely new aspects such as the combination of BNCT and XRT, the CT guidance for radiotherapy doses and the role of radiosensitizers localization in the tissues and cells during the double-radiotherapy treatment, ultimately leading to the expansion of the therapeutic window for several types of cancers with negative prognosis.

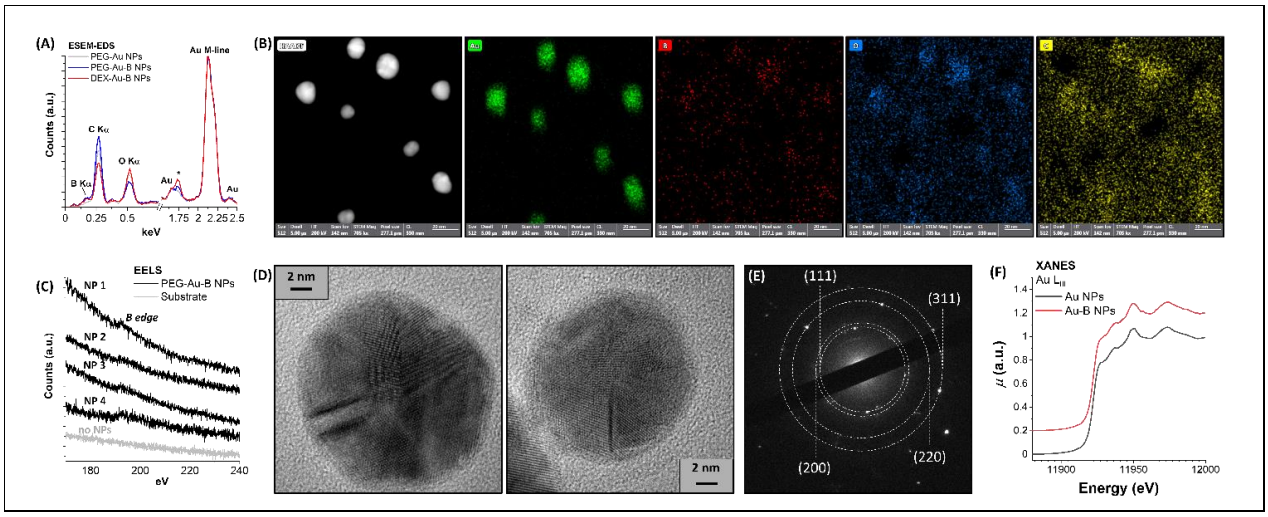

Figure 18: A) ESEM-EDX analysis of Au-B NPs. (B) STEM-EDX analysis of 5000 Da PEG-Au-B NPs. (C) EELS analysis on different 5000 Da PEG-Au-B NPs and on the TEM grid background between them. (D) HRTEM of 5000 Da PEG-Au-B NPs. (E) SAED on a group of 5000 Da PEG-Au-B NPs. (F) Au LIII-edge normalized XANES spectra of 5000 Da Au-B and Au NPs. The Au-B spectrum is shifted along the y axis for the sake of better visualization.

Publication: [Adv. Funct. Mater. 33 (2023), 2303366.]

Robust Molecular Anodes for Electrocatalytic Water Oxidation Based on Electropolymerized Molecular Cu Complexes

S. Amthor[1,+], K. Ranu[1,+], C. G. Bellido[1], F. F. Salomón[1], A. Piccioni[2], R. Mazzaro[2], F.o Boscherini[2], L. Pasquini[2], M. Gil Sepulcre[1], A. Llobet[1,3]*.*

[1] Institute of Chemical Research of Catalonia (ICIQ), Barcelona Institute of Science and Technology (BIST), Tarragona, Spain, Avinguda Països Catalans 16, 43007 Tarragona, Spain.

[2] Department of Physics and Astronomy, Alma Mater Studiorum – Università di Bologna, viale C. Berti Pichat 6/2, 40127 Bologna, Italy

[3] Departament de Química, Universitat Autònoma de Barcelona, 08193 Cerdanyola del Vallès, Barcelona, Spain.

Solar water splitting is among the most appealing approaches to boost the current energetic transition to renewable sources, but faces the dire need for the development of robust catalyst, to be efficiently anchored on conductive and/or semiconductive substrate for device integration. While molecular catalysts based on transition metal complexes are displaying unique tunability of functional properties, in-situ reconstruction to the corresponding metal is almost invariably occurring under water splitting-relevant operating conditions, with few significant exceptions like $[LCu]^{2-}$ class of copper-based complex, unambiguously demonstrated to be stable in its molecular in nature at pH 7 while promoting water oxidation to molecular oxygen.

In this work, a homologue that could be anchored by electropolymerisation on conductive and/or semiconductive surfaces was developed, by placing a thiophene group at the macrocyclic ligand backbone, without modifying the intrinsic electronic properties of the original metal center. The local structure around the Cu metal center was studied by X-ray absorption spectroscopy (XAS) at the Cu K edge, including X-ray absorption near edge structure (XANES) and extended X-ray absorption fine structure (EXAFS). The $[LCu]^{2-}$ was characterized before and after the electropolimerization on the conductive surface, made of a glassy carbon electrode containing multi-walled carbon nanotubes (GC/CNT). The XANES spectrum of $[LCu]^{2-}$ before the electropolimerization exhibits the absorption edge at about 8985 eV, matching very well the parent, non-thiophene substituted complex $[(Mac)CuII]^{2-}$.[1] This agreement confirms that the two complexes are characterized by the same Cu(II) oxidation state. The analysis of the EXAFS signal yields a Cu-N average distance of ≈1.88 Å, which is compatible with the value of ≈1.90 Å previously determined from the EXAFS analysis of the parent $[(Mac)CuII]^{2-}$ complex.[1] After the electropolimerization, the pristine new complex labelled as GC/CNT@p-$[LCu]^{2-}$ 0h exhibits the same spectral features, indicating that the oxidation state II of the metal center and its coordination environment do not change upon electropolymerization. In order to elucidate the long-term stability of the molecular hybrid material GC/CNT@p-$[LCu]^{2-}$, a controlled potential electrolysis (CPE) experiment at an E_{app} = 1.3 V was conducted for 24 h. To check the stability of the molecular hybrid material during the electrocatalytic process, XANES and EXFAS were also carried out after different CPE times (1, 6, and 24 h), showing identical features to those of $[LCu]^{2-}$ and pristine GC/CNT@p-$[LCu]^{2-}$ 0 h and indicating that the Cu(II) oxidation state and the local structure do not change.

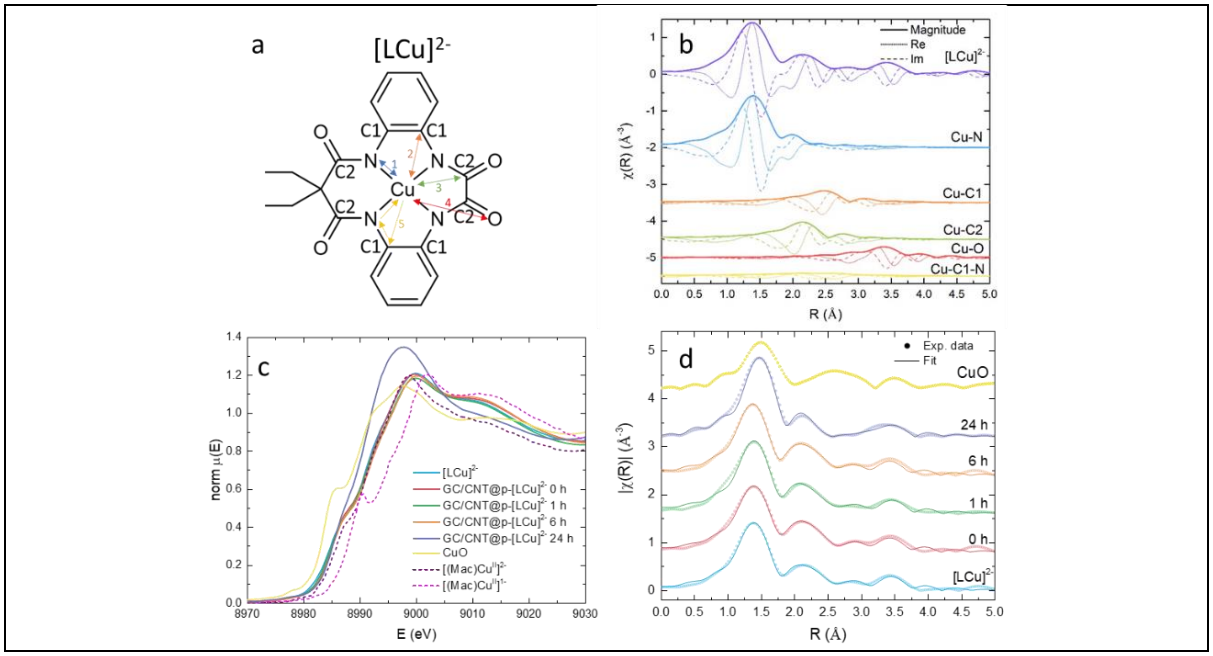

Figure 19: : a: Geometry of [LCu]$^{2-}$ scattering paths used for fitting the EXAFS spectra. b: Example of the Fourier transform of each scattering path that gives a significant contribution to the final . c: Normalized Cu K-edge XANES of [LCu]2− and electropolymerized GC/CNT@p-[LCu]2− both pristine (0 h) and after different CPE times. The XANES spectra of the non-thiophene substituted counterpart [(Mac)CuII)]2− and of its oxidized form [(Mac)CuIII]− are also shown. d: Experimental Fourier transforms of k2-weighted EXAFS spectra (dots) of [LCu]2− and electropolymerized GC/CNT@p-[LCu]2− samples. The XANES and EXAFS spectra of a CuO reference sample are reported for the sake of comparison.

Differently, the XANES spectrum of sample GC/CNT@p-[LCu]$^{2-}$ 24 h displays a blue shift of the absorption edge by ≈0.5 eV, together with a broadening of the white line. Even if a shift in the absorption energy suggests an increase of the oxidation state, the present energy shift is below the threshold indicated for the full transition from Cu(II) to Cu(III), usually in the range between 1 and 2 eV. Comparing the FT-EXAFS spectra of GC/CNT@p-[LCu]$^{2-}$ 24 h with pristine [LCu]$^{2-}$, a shift of the first shell peak can be noticed, corresponding to an expansion of the Cu-N nearest neighbor distance from ≈1.88 Å in [LCu]$^{2-}$ to ≈1.95 Å. This contrasts with the idea of increased oxidation state, which should result in a contraction of the Cu–N distance. Therefore, it is more likely that the observed changes in XANES and EXAFS spectra arise from a distortion of the macrocyclic ligand rather than a change of oxidation state from Cu(II) to Cu(III).[2]

References:

[1] P. Garrido-Barros, D. Moonshiram, M. Gil-Sepulcre, P. Pelosin, C. Gimbert-Suriñach, J. Benet-Buchholz, A. Llobet, *J. Am. Chem. Soc.* 2020, *142*, 17434.

[2] S. Amthor, K. Ranu, C. G. Bellido, F. F. Salomón, A. Piccioni, R. Mazzaro, F. Boscherini, L. Pasquini, M. Gil-Sepulcre, A. Llobet, *Adv. Mater.* 2023, *2308392*

Year 2023 Publications

1. Bacchella, C. et al. Copper Binding and Redox Activity of α-Synuclein in Membrane-Like Environment. Biomolecules 13, 287 (2023).
2. Cámara, F. et al. Piccoliite, NaCaMn3+2(AsO4)2O(OH), a new arsenate from the manganese deposits of Montaldo di Mondovì and Valletta, Piedmont, Italy. Mineralogical Magazine 87, 204–217 (2023).
3. Ghorbani, E. et al. Elucidating the local structure of V substitutes in In2S3 as potential intermediate band material by x-ray absorption spectroscopy and first principles calculations. J. Phys. Energy 5, 035003 (2023).
4. Monico, L. et al. Total electron yield (TEY) detection mode Cr K-edge XANES spectroscopy as a direct method to probe the composition of the surface of darkened chrome yellow (PbCr1-xSxO4) and potassium chromate paints. Nuclear Instruments and Methods in Physics Research Section B: Beam Interactions with Materials and Atoms 539, 141–147 (2023).
5. Ritter, K. et al. Atomic scale structure and bond stretching force constants in stoichiometric and off-stoichiometric kesterites. The Journal of Chemical Physics 159, 154705 (2023).
6. Xu, M. et al. Giant uniaxial negative thermal expansion in FeZr2 alloy over a wide temperature range. Nat Commun 14, 4439 (2023).
7. Amatori, S. et al. Gold nanorods derivatized with CTAB and hydroquinone or ascorbic acid: spectroscopic investigation of anisotropic nanoparticles of different shapes and sizes. Nanoscale Advances 5, 3924–3933 (2023).
8. Amthor, S. et al. Robust Molecular Anodes for Electrocatalytic Water Oxidation Based on Electropolymerized Molecular Cu Complexes. Advanced Materials, 2308392 (2023).
9. Chinnappa Chinnabathini, V. et al. Gas phase deposition of well-defined bimetallic gold-silver clusters for photocatalytic applications. Nanoscale 15, 6696–6708 (2023).
10. Goudjil, M. et al. Synthesis and characterization of AsO[(W,Mo)O3]13, a new (6)-intergrowth tungsten bronze (ITB). Journal of Solid State Chemistry 322, 123987 (2023).
11. Joubert, J.-M. et al. Site occupancies in a chemically complex σ-phase from the high-entropy Cr–Mn–Fe–Co–Ni system. Acta Materialia 259, 119277 (2023).
12. Meekel, E. G. et al. Truchet-tile structure of a topologically aperiodic metal–organic framework. Science 379, 357–361 (2023).
13. Scaramuzza, S. et al. A Laser Synthesis Route to Boron-Doped Gold Nanoparticles Designed for X-Ray Radiotherapy and Boron Neutron Capture Therapy Assisted by CT Imaging. Advanced Functional Materials 33, 2303366 (2023).
14. Virga, S. et al., Structural Features Governing the Near-Edge X-ray Absorption Spectra of Lead Halide Perovskites. J. Phys. Chem. C 127, 18058–18066 (2023).
15. G. Romolini, L. Sun, E. Fron, F. d'Acapito, D. Grandjean, M. B. Roeffaers, C. Martìn, J. Hofkens, Single Atom Silver-Phosphors in Titanosilicate Matrix for Enhanced LED Applications. *Adv. Optical Mater.* 2023, 2301894.
16. S. Laureti, F. d'Acapito, P. Imperatori, E. Patrizi, G. Varvaro, A. Puri, C. Cannas and A. Capobianchi "Synthesis of highly ordered L10 MPt alloys (M = Fe, Co, Ni) from crystalline salts: an in situ study of the pre-ordered precursor reduction strategy", J. Mater. Chem. C, 2023,11, 16661-16671.

Contacts

Beamline responsible:
Francesco d'Acapito: dacapito@esrf.fr, +33 4 7688 2426, +33 6 8936 4302
Beamline scientists:
Alessandro Puri: puri@esrf.fr, +33 4 7688 2859
Jacopo Orsilli: jacopo.orsilli@esrf.fr, +33 4 7688 2530
Technical Services :
Fabrizio La Manna, lamanna@esrf.fr, +33 4 7688 2962

Beamline: +33 4 7688 2085
Laboratory: +33 4 7688 2743
Skype: LISA_beamline@EBS
Mattermost: @opd08

Web page: http://www.esrf.eu/UsersAndScience/Experiments/CRG/BM08/

Forthcoming proposals submission deadlines
ESRF quota: March 4th, 2024.
CERIC quota: early 2024, date to be announced.

Contributors to this issue

F. d'Acapito, J. Orsilli (Uni Mi Bicocca), A. Puri (CNR-IOM), A. Fantin (HZB Berlin), P. Ghigna (Uni Pv), L. Monico (CNR-ISTEC), A. Sanson (Uni Pd), R. Mazzaro (Uni Bo), S. Amatori and G. Iucci (Uni Roma Tre), M. Ciani, S. Margheri and G. O. Lepore (Uni Fi), E. Petsali and M. Katsikini (Uni Tessaloniki), R. E. Russo and G. Giuli (Uni Camerino).